

1           **Improved parameterization of snow albedo in WRF + Noah. Part II:**

2                   **Applicability to snow estimates for the Tibetan Plateau**

3   **Lian Liu<sup>1,2</sup>, Yaoming Ma<sup>1,2,3,4</sup>, Massimo Menenti<sup>5,6</sup>, Rongmingzhu Su<sup>1,2,4</sup>, Nan**  
4   **Yao<sup>1,2,4</sup>, Weiqiang Ma<sup>1,2,3</sup>**

5   [1] {Key Laboratory of Tibetan Environment Changes and Land Surface Processes,  
6   Institute of Tibetan Plateau Research, Chinese Academy of Sciences, Beijing, 100101,  
7   China}

8   [2] {Land Atmosphere Interaction and its Climatic Effects Group, State Key Laboratory  
9   of Tibetan Plateau Earth System Science, Institute of Tibetan Plateau Research, Chinese  
10   Academy of Sciences, Beijing, 100101, China}

11   [3] {CAS Center for Excellence in Tibetan Plateau Earth Sciences, Beijing, 100101,  
12   China}

13   [4] {University of Chinese Academy of Sciences, Beijing 100049, China}

14   [5] {State Key Laboratory of Remote Sensing Science, Institute of Remote Sensing and  
15   Digital Earth, Chinese Academy of Sciences, Beijing, 100101, China}

16   [6] {Delft University of Technology, Delft, Netherlands}

17   Correspondence to: Y. M. Ma ([ymma@itpcas.ac.cn](mailto:ymma@itpcas.ac.cn))

18

19 **Abstract**

20 Snow albedo is important to the land surface energy balance and to the water cycle.  
21 During snowfall and subsequent snowmelt, snow albedo is usually parameterized as  
22 functions of snow related variables in land surface models. However, the default snow  
23 albedo scheme in the widely used Noah land surface model shows evident shortcomings  
24 in land-atmosphere interactions estimates during snow events on the Tibetan Plateau.  
25 Here, we demonstrate that our improved snow albedo scheme performs well after  
26 including snow depth as an additional factor. By coupling the WRF and Noah models,  
27 this study comprehensively evaluates the performance of the improved snow albedo  
28 scheme in simulating eight snow events on the Tibetan Plateau. The modeling results  
29 are compared with WRF run with the default Noah scheme and in situ observations.  
30 The improved snow albedo scheme significantly outperforms the default Noah scheme  
31 in relation to air temperature, albedo and sensible heat flux estimates, by alleviating  
32 cold bias estimates, albedo overestimates and sensible heat flux underestimates,  
33 respectively. This in turn contributes to more accurate reproductions of snow event  
34 evolution. The averaged RMSE relative reductions (and relative increase in correlation  
35 coefficients) for air temperature, albedo, sensible heat flux and snow depth reach 27 %  
36 (5 %), 32 % (69 %), 13 % (17 %) and 21 % (108 %) respectively. These results  
37 demonstrate the strong potential of our improved snow albedo parameterization scheme  
38 for snow event simulations on the Tibetan Plateau. Our study provides a theoretical  
39 reference for researchers committed to further improving the snow albedo  
40 parameterization scheme.

41 **Keywords:** WRF; snow albedo parameterization; turbulent heat and vapor fluxes;  
42 Tibetan Plateau

43

## 44 **1 Introduction**

45 The surface albedo directly determines the proportion of incident solar radiation that is  
46 absorbed by the surface, and is an important parameter in climate and land surface  
47 models (LSMs) (Sellers et al., 1996). Small changes in surface albedo can affect the  
48 energy balance in the land-atmosphere system, and can drive both local and global  
49 climate change (Bloch, 1964).

50 Surface albedo changes dramatically during snowfall and snowmelt cycles. Much  
51 research has been carried out to identify the factors that influence these changes,  
52 including the effects of terrain shielding, altitude, sky conditions, vegetation, and snow  
53 properties such as grain size, liquid water content, depth, and impurities (Warren and  
54 Wiscombe, 1980; Wiscombe and Warren, 1980; Aoki et al., 2003; Jonsell et al., 2003;  
55 Hansen and Nazarenko, 2004; Liang et al., 2005; Wang et al., 2015; He et al., 2018a).  
56 This body of research has led to the development of many parameterization schemes  
57 for surface albedo (Oerlemans and Knap, 1998; Wang et al., 2007; Bao et al., 2008; Li  
58 and Hu, 2009; Gardner and Sharp, 2010; Kuipers Munneke et al., 2011; Malik et al.,  
59 2014; Dang et al., 2015; He et al., 2017, 2018b; Meng and Li, 2019; Saito et al., 2019;  
60 Wang et al., 2020). Most snow albedo parameterization schemes depend on statistical  
61 empirical formulas and constant parameters, rather than representing physical snow-  
62 albedo feedback processes. To improve the performance of snow albedo  
63 parameterization schemes for simulating land-atmosphere interactions, Bao and Lyu  
64 (2009) added consideration of solar zenith angle to a regional climate model, which  
65 resulted in a 1.2 °C temperature increase, and considerably improved the cold bias in  
66 East Asia and improved the representation of diurnal ground temperature changes in  
67 northwest China. Park and Park (2016) investigated the effect of vegetation on snow  
68 covered surface albedo and improved the winter surface albedo estimates from their  
69 LSM by including leaf and stem indices in the snow albedo parameterization scheme,  
70 which reduced the root mean square error (RMSE) by 69 %. Zhong et al. (2017)  
71 considered aerosol radiative effects on snow processes in their simulations and

72 successfully reproduced the snow albedo and snow depth. Fresh snow albedo depends  
73 on snow depth, and albedo parameterization schemes that fail to account for this  
74 generally overestimate the snow depth. To address this, Wang et al. (2020) developed a  
75 new albedo scheme for fresh snow, which accounts for the relationship between fresh  
76 snow albedo, snow grain size and snow depth, resulting in improved snow depth  
77 estimates during the snow ablation period on the Tibetan Plateau. This highlights the  
78 importance of accounting for the effect of snow depth on fresh snow albedo.

79 A coupled land-atmosphere model can provide useful insights into conditions on the  
80 Tibetan Plateau, where the terrain is complex and there are few, and unevenly  
81 distributed observation stations (Maussion et al., 2011; Yuan et al., 2016; Norris et al.,  
82 2017; Bonekamp et al., 2018; Rahimi et al., 2019). However, the parameterization  
83 scheme for surface albedo in the Noah LSM, which is currently the most widely used  
84 LSM, does not account for all the factors that influence albedo. It includes many  
85 predetermined parameters and an approximate treatment of vegetation, soil and snow,  
86 which can result in some inaccuracies in the estimated surface albedo (Wen et al., 2011;  
87 Liu et al., 2019). For example, the surface albedo parameterization scheme in the Noah  
88 LSM considers snow cover and age, but ignores other snow related factors, such as  
89 snow depth, that can drive dramatic changes in albedo (Ek et al., 2003). This makes it  
90 inappropriate to use the Noah LSM to characterize changes in snow albedo that follow  
91 from snowfall and melt processes in complex topographic areas. However, the Noah  
92 LSM appears to be the most readily available snow albedo scheme for long term climate  
93 modeling research (Rai et al., 2019). Despite its shortcomings, the Noah albedo  
94 parameterization scheme does provide substantial improvements to estimates of the  
95 magnitude and timing of both the peak snowfall amount and the maximum snow cover  
96 extent, following from the scheme's consideration of snow albedo decay and liquid  
97 water refreezing (Livneh et al., 2010). The above issues represent opportunities for  
98 improvements to be made to the snow albedo parameterization scheme in the Noah  
99 LSM.

100 The use of an advanced snow albedo parameterization scheme is crucial for accurate  
101 estimation of land-atmosphere interactions over the Tibetan Plateau, where the snow-  
102 albedo effect is extremely strong. It has been shown that the Weather Research and  
103 Forecasting (WRF; Skamarock et al., 2008) model, when coupled with the default Noah  
104 albedo parameterization scheme, results in an apparent cold bias over the Tibetan  
105 Plateau (Gao et al., 2015; Meng et al., 2018; Liu et al., 2019). This bias can be reduced  
106 by including albedo products from the Moderate Resolution Imaging  
107 Spectroradiometer (MODIS) and an additional snow depth parameter as independent  
108 variables in the Noah albedo parameterization scheme (Liu, 2020). This approach is not  
109 the same as assimilating satellite retrieved snow related products into the LSM, which  
110 has also been shown to lead to improvements (Xu and Shu, 2014; Zhang et al., 2014;  
111 Lin et al., 2016; Xue et al., 2019). This improved snow albedo scheme has been  
112 successfully implemented in the WRF model, coupled with Noah, to simulate land-  
113 atmosphere interactions during a regional heavy snow event on the Tibetan Plateau (Liu,  
114 2020). However, it has not been shown that the improvements that follow from the  
115 improved snow albedo scheme are universal over the Tibetan Plateau, and this should  
116 be studied further. Severe snowfall occurs often over the southern Tibetan Plateau,  
117 while snowfall over the eastern Tibetan Plateau is generally of relatively weak intensity,  
118 and the rate of snowmelt varies widely depending on the heterogeneous underlying  
119 surfaces. This makes it necessary to carry out numerical experiments that focus on snow  
120 events over the eastern and southern Tibetan Plateau to assess how reliably the  
121 improved scheme can be used to characterize different snowfall intensities and  
122 snowmelt processes.

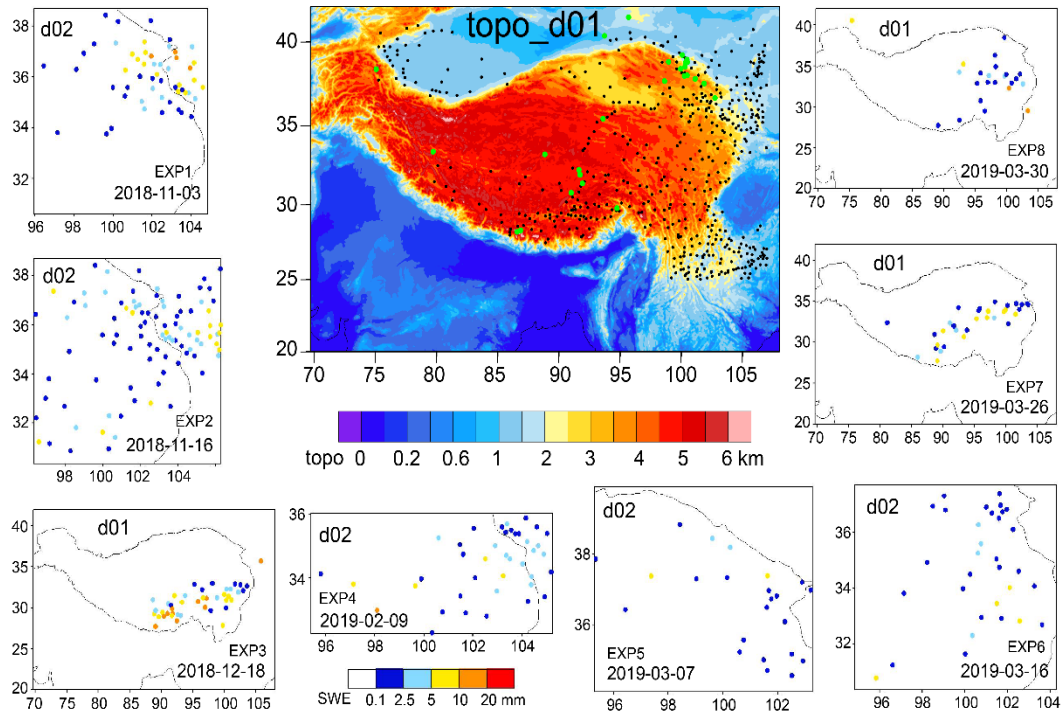
123 In this study, we selected eight moderate to snowstorm events that occurred over the  
124 southern and eastern Tibetan Plateau to assess the universality of the improvements  
125 offered by our improved snow albedo scheme in WRF coupled with the Noah LSM.  
126 For each snow event, two numerical experiments were carried out: one implementing  
127 the default Noah snow albedo scheme, and the other implementing our improved snow  
128 albedo scheme. The model performance was assessed through comparison of the

129 modeled air temperature, albedo, snow depth, turbulent heat and vapor fluxes with  
130 ground observations. The aim of this study is to explore the potential of our improved  
131 snow albedo parameterization scheme to simulate snow events over the whole Tibetan  
132 Plateau more accurately than can be done using the standard default scheme. We hope  
133 that this study will also provide a useful reference for researchers working to develop  
134 and improve this, and other albedo parameterization schemes.

## 135 **2 Data and methodology**

### 136 **2.1 Description of snow events**

137 We selected China Meteorological Administration (CMA) national observation stations  
138 on the Tibetan Plateau, and in the surrounding regions, with elevations exceeding 1000  
139 m. This resulted in a total of 502 stations (Figure 1 shows their distribution). Snowfall  
140 events were identified from the hourly air temperature and precipitation observations  
141 from all 502 stations when the air temperature was below 0 °C. Daily snowfall amounts  
142 were calculated, using 08:00 Beijing Standard Time (BST) as the start and end time for  
143 each day. The standards to define snowfall grade were taken from the China  
144 Meteorological Standardization Network (<http://www.cmastd.cn/>). Using these  
145 standards, eight different grades of snowfall event were considered in our study,  
146 including moderate, heavy and snowstorm. Most of the snowfall events took place over  
147 the eastern Tibetan Plateau, and some occurred in a large region across the southern and  
148 central to the eastern Tibetan Plateau. The maximum daily snowfall amount from all  
149 snowfall events exceeded 8 mm, and four events resulted in more than 10 mm daily  
150 snowfall, making these snowstorm grade events. Snow depth is much greater on the  
151 southern Tibetan Plateau (> 50 cm) than it is on the eastern and central Tibetan Plateau  
152 (<=20 cm). The description of eight snowfall events, including the date and location of  
153 moderate to snowstorm grade events, the maximum snow depth and daily snowfall  
154 amount, are detailed in Table 1. The daily snowfall amounts from the eight snowfall  
155 events are shown in Figure 1.



156

157 **Figure 1.** WRF domains of d01 and d02, and CMA observations of daily snowfall  
 158 amount in color solid circles for the eight experiments. The topographical height of d01  
 159 is shaded with black solid circles indicating the locations of the CMA stations, and  
 160 green solid circles indicating the locations of the CAS stations and the Qilian Mountains  
 161 integrated observatory network.

162

163

164

165

166

167

168

169

170 **Table 1** Description of eight snowfall events using China Meteorological  
 171 Administration observations.

Snow events	Event 1	Event 2	Event 3	Event 4	Event 5	Event 6	Event 7	Event 8
Date of moderate to snowstorm	Nov. 3-6, 2018	Nov. 15-17, 2018	Dec. 17-18, 2018	Feb. 9, 2019	Mar. 7-8, 2019	Mar. 16, 2019	Mar. 26, 2019	Mar. 30-Apr. 1, 2019
Region in the Tibetan Plateau	eastern	eastern	southern, central, eastern	eastern	eastern	eastern	southern, central, eastern	central, eastern
Maximum daily snowfall amount (unit: mm)	13.6	9.2	18.7	11	9.3	9.1	8.7	14.3
Maximum snow depth (unit: cm)	18	16	65	20	13	9	53	18

172 **2.2 Model description and experiment configuration**

173 The WRF model (Skamarock et al., 2008), version 3.7.1, coupled with the Noah LSM,  
 174 was used to simulate the eight snowfall events in this study. It is a fully compressible,  
 175 non-hydrostatic model and includes a run time hydrostatic option. Vertical levels are  
 176 determined using a mass based terrain following hydrostatic pressure coordinate, and  
 177 calculations are performed on an Arakawa C grid. The model uses 2<sup>nd</sup> and 3<sup>rd</sup> order  
 178 Runge-Kutta time integration schemes, and 2<sup>nd</sup> to 6<sup>th</sup> order advection schemes in both  
 179 the horizontal and vertical direction.

180 The extremely steep terrain on the central and southern Tibetan Plateau led to model  
 181 instability and failure for snowfall events 3, 7 and 8 when a relatively fine horizontal  
 182 resolution of 1 km was used; however, the calculations remained stable when the  
 183 resolution was increased to 5 km. *We therefore used two ways nested modeling domains*

184 in our model configuration for snowfall events 1, 2, 4, 5 and 6, and a single modeling  
185 domain for snowfall events 3, 7 and 8. The coarse domain (d01) was used to simulate  
186 synoptic scale atmospheric conditions over 20.0-42.0° N and 69.7-108.0° E with a  
187 horizontal resolution of 5 km. The inner domain (d02) had a horizontal resolution of 1  
188 km, and event 1 occupied  $876 \times 966$  grid cells, event 2 occupied  $976 \times 1001$  cells, event  
189 4 was resolved by  $966 \times 451$  cells, event 5 was calculated over  $781 \times 686$  cells, and  
190 event 6 covered  $926 \times 881$  cells. The vertical structure of both domains included 35  
191 unevenly spaced layers and extended up to 50 hPa. The model was configured to use  
192 the Noah LSM in d01 and d02 to describe all land-atmosphere interactions; the  
193 Thompson scheme to represent microphysical processes; the Dudhia scheme to  
194 represent shortwave radiation, the RRTM scheme to describe longwave radiation; the  
195 YSU scheme to describe the planetary boundary layer; and only in d01 to use the Kain-  
196 Fritsch cumulus parameterization scheme for clouds.

197 We conducted numerical experiments to simulate snow event 1 (EXP1), event 2 (EXP2),  
198 event 3 (EXP3), event 4 (EXP4), event 5 (EXP5), event 6 (EXP6), event 7 (EXP7) and  
199 event 8 (EXP8). The model domains for the experiments are shown in Figure 1. Each  
200 experiment included two model simulations: one implementing the default Noah snow  
201 albedo parameterization scheme, and the other implementing a new improved snow  
202 albedo scheme. *The new improved snow albedo was developed based on conversion*  
203 *formula from MODIS narrowband spectral reflectance to broadband albedo following*  
204 *Liang (2000) and albedo calculation formula about fresh snow, firn and bare ground*  
205 *albedo, snow age and depth following Oerlemans and Knap (1998). MODIS broadband*  
206 *albedo and WRF modeled snow depth and age were used to estimate the related*  
207 *parameters i.e., firn albedo and scales of snow depth and age through nonlinear fitting*  
208 *of the above albedo calculation formula. The final nonlinear fitting results produced*  
209 *the new improved snow albedo scheme, seeing the equations (3) and (4). The snow*  
210 albedo is parameterized using Eq. (1) and (2) in the default Noah land surface scheme  
211 (Livneh et al., 2010), and using Eq. (3) and (4) in the improved scheme (Liu, 2020):

212

$$\alpha_{\text{snow}} = \alpha_{\text{max}} \times A^{t^B} \quad (1)$$

$$\alpha = \alpha_{bg} + sc \times (\alpha_{\text{snow}} - \alpha_{bg}) \quad (2)$$

$$\alpha_{\text{snow}} = 0.13 + 0.66e^{\left(\frac{t}{1.38}\right)} \quad (3)$$

$$\alpha = \alpha_{\text{snow}} + (0.19 - \alpha_{\text{snow}})e^{\left(\frac{-d}{0.11}\right)} \quad (4)$$

215 where A and B are constants, equal to 0.94 and 0.58, respectively, for snow  
216 accumulation periods, and are 0.82 and 0.46, respectively, for other periods;  $\alpha_{bg}$  is the  
217 background albedo, which depends on the land cover type;  $sc$  is snow cover, and  
218 ranges from 0 to 1;  $\alpha_{\text{max}}$  is fresh snow albedo;  $\alpha_{\text{snow}}$  is snow albedo;  $t$  is the snow  
219 age in units of days;  $d$  is snow depth in meters.

220 The fifth generation European Centre for Medium Range Weather Forecasts (ECMWF)  
221 reanalysis dataset (ERA5), with a spatial resolution of  $0.25^\circ \times 0.25^\circ$  and 3 h temporal  
222 resolution, provided initial and boundary conditions for our numerical experiments. The  
223 ERA data were calculated using 4DVar data assimilation in CY41R2 from ECMWF's  
224 Integrated Forecast System, with 137 vertical hybrid sigma/pressure levels, extending  
225 to 0.01 hPa. ERA5 is freely available from the website  
226 <https://www.ecmwf.int/en/forecasts/datasets/reanalysis-datasets/era5>. The near real  
227 time MODIS land cover product was used to replace the outdated land cover in WRF  
228 preprocessing system. We ran the model from before the onset of each snowfall event  
229 until and after all snowmelt following the event had ceased. EXP1 was run Nov. 1-8  
230 2018, EXP2 was run Nov. 13-18 2018, EXP3 was run Dec. 16-20 2018, EXP4 was run  
231 Feb. 5-11 2019, EXP5 was run Mar. 2-10 2019, EXP6 was run Mar. 12-18 2019, EXP7  
232 was run Mar. 24-29 2019, EXP8 was run Mar. 28-Apr.7 2019. The model results were  
233 output at 3 hours intervals and the first day was used for model spin up.

### 234 **2.3 Data for model evaluation and comparison**

235 CMA hourly observations of air temperature and snow depth from 502 stations were

236 used to assess the WRF model estimates of 2 m air temperature and snow depth that  
237 were made using the improved snow albedo parameterization scheme. Albedo is a key  
238 factor for net radiation calculations, and is defined as the ratio of reflected shortwave  
239 radiation (upwards) to received shortwave radiation (downwards). It determines the  
240 distribution of turbulent land surface heat fluxes between sensible (SH) and latent heat  
241 (LH). There are many meteorological observations available that have been  
242 continuously recorded on the Tibetan Plateau at atmospheric boundary layer towers,  
243 eddy covariance systems (Ma et al., 2018, 2020) and the Qilian Mountains integrated  
244 observatory network (Li, 2019; Liu et al., 2020; Zhao and Zhang, 2020). These provide  
245 in situ data that are assumed to constitute ‘truth’ for the model validation in this study.  
246 In situ observations of albedo, SH and LH from 11 Chinese Academy of Sciences (CAS)  
247 stations/samples, and from 16 stations in the Qilian Mountains integrated observatory  
248 network are used to evaluate the accuracy of the improved snow albedo  
249 parameterization scheme for modeling snow events on the Tibetan Plateau. It is  
250 reasonable to compare observations of albedo, SH and LH with model estimates at 5  
251 km resolution because there are only a few in situ observation stations in d02, but a  
252 total of 27 observation stations in d01. At local solar noon in Lhasa (14:00 BST), the  
253 observed albedo value is closer to the Lambertian albedo that is described by the WRF  
254 model when coupled with LSMs. We therefore used albedo observations made at 14:00  
255 BST to evaluate the model calculated albedo. Quality control codes 1, 2 and 3 were  
256 selected when using the Turbulence Knight version 3 (TK3) software, and 0 was used  
257 when using the Eddypro software to calculate SH and LH. Details of the 27 stations  
258 from the CAS and the Qilian Mountains integrated observatory network that were used  
259 in our study are provided in Table 2, and their locations on the Tibetan Plateau are  
260 shown in Figure 1. *In order to compare WRF simulations against in situ observations,*  
261 *sampling the gridded model estimates and interpolating to given ground stations’*  
262 *locations were done by bi-linear interpolation of the four surrounding model grid points.*  
263 The RMSE and the correlation coefficient were calculated for the assessment of the  
264 model performance in relation to albedo, air temperature, SH, LH, and snow depth

265 estimates.

266 **Table 2** Location of stations from the Chinese Academy of Sciences (CAS) and the  
267 Qilian Mountains integrated observatory network, and whether or not observations of  
268 albedo, SH and LH were used from each station.

Station No.	Station Name	Station Type	Latitude (° N)	Longitude (° E)	Elevation (m)	Using albedo	Using SH and LH
1	SETS	CAS	29.77	94.73	3326	Yes	No
2	QOMS	CAS	28.21	86.56	4276	Yes	Yes
3	QOMS sample	CAS	28.31	86.85	4600	No	Yes
4	MASWE	CAS	38.41	75.05	3668	Yes	No
5	Nam Co	CAS	30.77	90.99	4730	Yes	Yes
6	NASDE	CAS	33.39	79.70	4264	Yes	No
7	Shuanghu	CAS	33.22	88.83	4947	Yes	Yes
8	NewD66	CAS	35.43	93.59	4465	Yes	No
9	BJ	CAS	31.37	91.90	4509	Yes	Yes
10	MS3478	CAS	31.93	91.71	4620	Yes	No
11	Amdo	CAS	32.24	91.62	4695	Yes	No
12	Yakou	Qilian	38.01	100.24	4148	Yes	Yes
13	Arou	Qilian	38.05	100.46	3033	Yes	Yes
14	Jingyangling	Qilian	37.84	101.12	3750	Yes	Yes
15	Dashalong	Qilian	38.84	98.94	3739	Yes	Yes
16	Heihe Remote Sensing	Qilian	38.83	100.48	1560	Yes	No
17	Huazhaizi Desert Steppe	Qilian	38.77	100.32	1731	Yes	Yes
18	Daman	Qilian	38.86	100.37	1556	Yes	Yes
19	Zhangye wetland	Qilian	38.96	100.45	1460	Yes	Yes
20	Guazhou	Qilian	41.41	95.67	2014	Yes	Yes
21	Dayekou	Qilian	38.56	100.29	2703	Yes	No
22	Dunhuang	Qilian	40.35	93.71	993	Yes	No
23	Liancheng	Qilian	36.69	102.74	2903	Yes	No
24	Linze	Qilian	39.24	100.06	1402	Yes	No
25	Sidalong	Qilian	38.43	99.93	3146	Yes	No
26	Xiyinghe	Qilian	37.56	101.86	3616	Yes	No

---

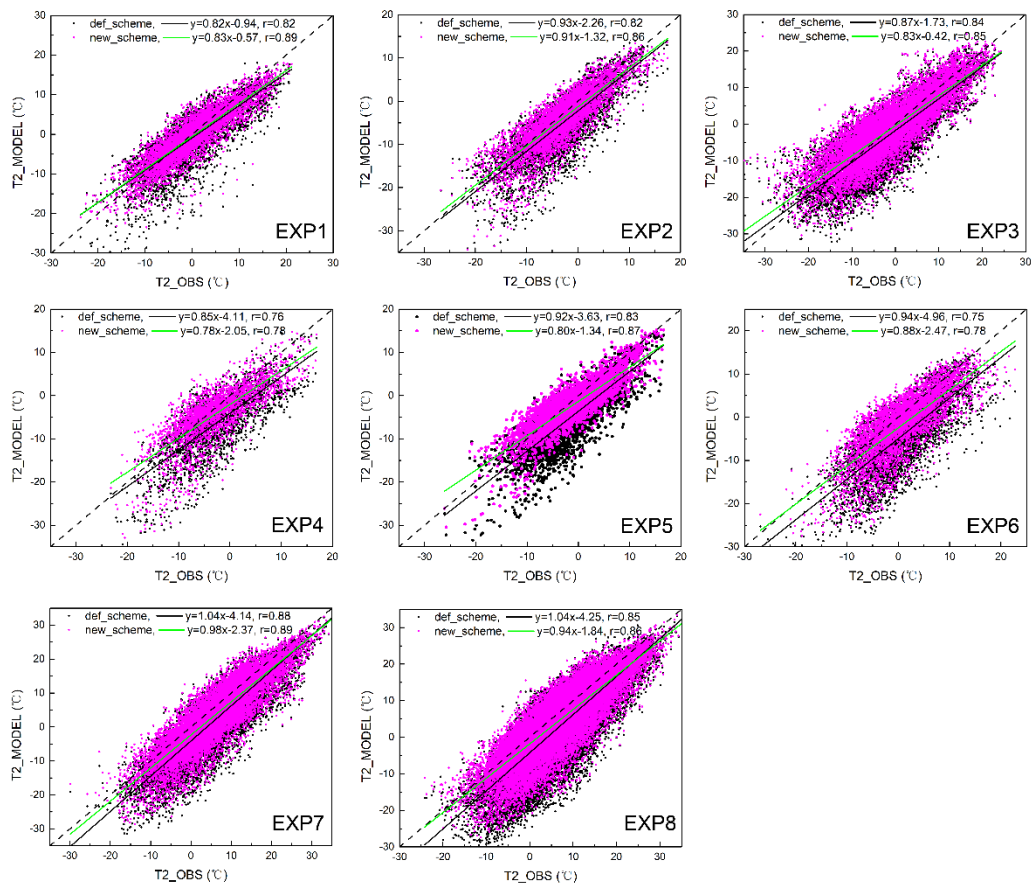
27	Tianjun	Qilian	37.70	98.61	3718	Yes	Yes
----	---------	--------	-------	-------	------	-----	-----

---

269 **3 Results**

270 **3.1 Air temperature**

271 Albedo is a key factor in determining the net radiation received at the surface, which  
272 determines the land surface energy balance and influences air temperature. Scatterplots  
273 of the air temperatures estimated by the WRF model and observed at the CMA stations  
274 are shown in Figure 2. *In all eight modeling experiments, implementing the improved*  
275 *snow albedo scheme in the WRF model greatly reduces the cold bias that occurs when*  
276 *the default Noah snow albedo scheme is used. Where the default Noah scheme results*  
277 *in a warm bias at the observed lower air temperature for EXP1 and EXP3, however,*  
278 *the improved albedo scheme does not improve the accuracy of the WRF estimates.*  
279 *Compared with cold bias caused by the default Noah albedo scheme at the observed*  
280 *lower air temperature, the improved snow albedo scheme results in a warm bias for*  
281 *EXP2, EXP4 and EXP5. On the whole, scatterplots comparing air temperature*  
282 *observations from CMA station with WRF estimates made using the improved snow*  
283 *albedo scheme estimates, show the data to be concentrated near the ideal fitting line,*  
284 *where the model has exactly reproduced the observations. Using the improved snow*  
285 *albedo scheme results in a marked reduction in the cold bias for the WRF model*  
286 *estimates for EXP1, EXP2, EXP4, EXP5 and EXP6, and the greatest reduction in the*  
287 *cold bias, for all eight experiments, occurs for EXP6 (Fig. 2).*



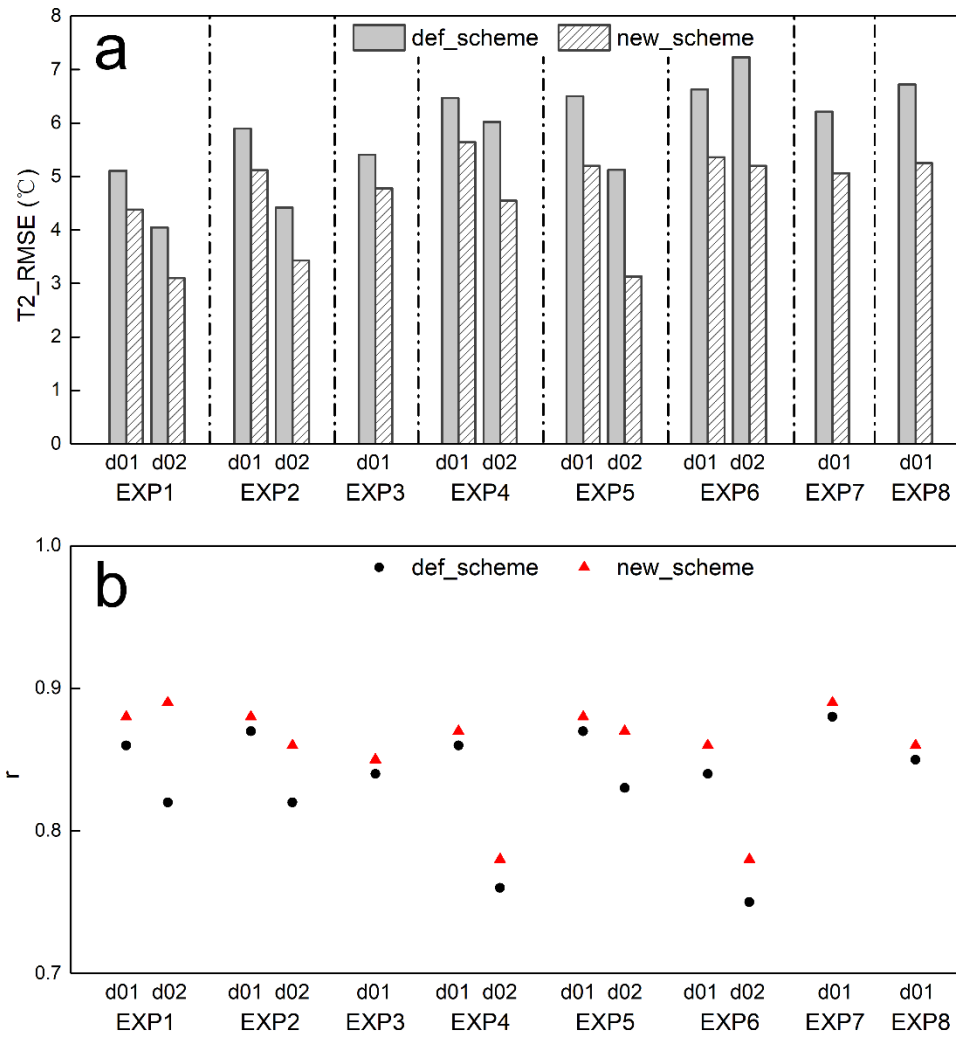
288

289 **Figure 2.** Scatterplot of air temperature, comparing the CMA observations and model  
 290 estimates for the eight experiments in the inner (high resolution) model domain from  
 291 WRF, using the default Noah snow albedo scheme (def\_scheme, black solid circle), and  
 292 using the improved snow albedo scheme (new\_scheme, red solid circle). The black  
 293 solid line is a linear fit to the black solid circles. The green solid line is a linear fit to  
 294 the red solid circles. The black dotted line is the line  $y=x$ .  $r$  is the correlation coefficient  
 295 between the CMA observations and the model estimates. The correlation coefficient ( $r$ )  
 296 is significant at 0.01 significance level.

297 To quantify the improvement to air temperature estimates that follows from  
 298 implementation of the improved snow albedo scheme, the RMSE and correlation  
 299 coefficient was calculated between CMA observations and model estimates of air  
 300 temperature, shown in Figure 3. The differences between the accuracy of the new  
 301 scheme and the default scheme are shown in Table 3. The accuracy of WRF air

302 temperature estimates varies between the different snowfall events, between the  
303 different snow albedo schemes, and also varies with model resolution. The lowest air  
304 temperature RMSE and the highest correlation coefficient are 3.1 °C and 0.89,  
305 respectively, and both occur for EXP1. The highest air temperature RMSE and the  
306 lowest correlation coefficient occur for EXP6, reaching 7.2 °C and 0.75, respectively.  
307 Air temperature RMSE generally ranges from 4.1 to 7.2 °C for the WRF estimates that  
308 were made using the default Noah snow albedo scheme estimates, with correlation  
309 coefficients ranging from 0.75 to 0.88. In contrast, when the improved snow albedo  
310 scheme is implemented in WRF, the RMSE ranges from 3.1 to 5.6 °C, and the  
311 correlation coefficients range from 0.78 to 0.89. *Compared with when the default Noah*  
312 *snow albedo scheme is used, the maximum decrease in air temperature RMSE when the*  
313 *new scheme is used reaches 2.03 °C, which represents an improvement of 28.1 %*, and  
314 the average decrease in air temperature RMSE is 1.2 °C, representing an improvement  
315 of 20.7 %. There is an improvement of more than 11 % in the RMSE for all eight  
316 experiments with the maximum improvement of 39 % when the new albedo scheme is  
317 used, relative to when the default scheme is used. Implementing the improved snow  
318 albedo scheme in WRF for all eight experiments also increased the correlation  
319 coefficient between observed and modeled air temperature, by 0.01-0.07, which  
320 represents an improvement of 1-9 % (Fig. 3, Table 3).

321 Compared with using the default Noah snow albedo scheme, using the improved  
322 scheme results in improved model estimates for all eight EXPs, decreasing the air  
323 temperature RMSE and increasing the correlation coefficient when compared with  
324 observations. These improvements occur for air temperature estimates calculated at  
325 both 5 km and 1 km resolution. The improvement to WRF model estimates is greater  
326 for calculations made at 1 km resolution than at 5 km resolution, and air temperature  
327 estimates are more accurate at 1 km resolution than at 5 km resolution *by implementing*  
328 *the improved albedo scheme* (Fig. 3, Table 3). Therefore, fine resolution (i.e., 1 km) is  
329 strongly recommended for future snowfall event modeling studies.



330

331 **Figure 3.** RMSE (a) and correlation coefficient (b) for air temperature (T2) between  
 332 observations and model estimates in d01 and d02. The correlation coefficient is  
 333 significant at the 0.01 significance level. For def\_scheme and new\_scheme, see Figure  
 334 2.

335

336

337

338

339 **Table 3** RMSE and correlation coefficient (r) for air temperature between CMA  
340 observations and model estimates, calculated using the default Noah snow albedo  
341 scheme (def\_scheme) and the improved albedo scheme (new\_scheme). The difference  
342 in RMSE is new\_scheme RMSE minus def\_scheme RMSE. The difference in r is  
343 new\_scheme r minus def\_scheme r. P value <0.05 is the significance test for the  
344 correlation.

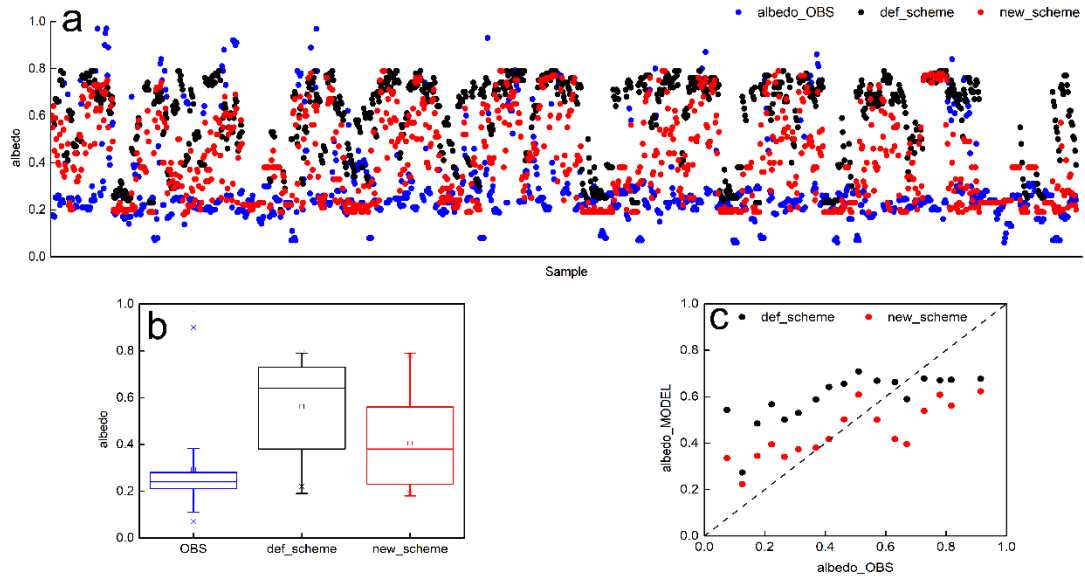
EXPs	Model Domain	RMSE (°C)				r			
		def_ scheme	new_ scheme	Difference	Relative Difference	def_ scheme	new_ scheme	Difference	Relative Difference
EXP1	d01	5.11	4.38	-0.73	-14.3 %	0.86	0.88	0.02	2.3 %
	d02	4.05	3.1	-0.95	-23.5 %	0.82	0.89	0.07	8.5 %
EXP2	d01	5.9	5.12	-0.78	-13.2 %	0.87	0.88	0.01	1.1 %
	d02	4.42	3.43	-0.99	-22.4 %	0.82	0.86	0.04	4.9 %
EXP3	d01	5.41	4.78	-0.63	-11.6 %	0.84	0.85	0.01	1.2 %
EXP4	d01	6.47	5.64	-0.83	-12.8 %	0.86	0.87	0.01	1.2 %
	d02	6.02	4.55	-1.47	-24.4 %	0.76	0.78	0.02	2.6 %
EXP5	d01	6.5	5.2	-1.30	-20.0 %	0.87	0.88	0.01	1.1 %
	d02	5.13	3.13	-2.00	-39.0 %	0.83	0.87	0.04	4.8 %
EXP6	d01	6.63	5.36	-1.27	-19.2 %	0.84	0.86	0.02	2.4 %
	d02	7.23	5.2	-2.03	-28.1 %	0.75	0.78	0.03	4.0 %
EXP7	d01	6.21	5.06	-1.15	-18.5 %	0.88	0.89	0.01	1.1 %
EXP8	d01	6.72	5.25	-1.47	-21.9 %	0.85	0.86	0.01	1.2 %

### 345 **3.2 Albedo**

346 Using the improved albedo scheme in the WRF model greatly reduces the cold air  
347 temperature bias that otherwise occurs, indicating an improvement to model  
348 performance. It is necessary to compare albedo estimates with in situ observations.  
349 There are very few observation stations located in the finer model domain, and so a  
350 total of 26 stations in d01 were used to evaluate the performance of the WRF

351 simulations of albedo at 5 km resolution (Table 2).

352 Scatterplots comparing observations and WRF estimates for albedo in the eight  
353 experiments, when both the default and improved snow albedo scheme were used, are  
354 shown alongside our statistical analysis in Figure 4. Albedo higher than 0.7 is  
355 interpreted as snowfall. Albedo in the range of 0.4 to 0.6 is interpreted as snowmelt.  
356 Albedo lower than 0.3 indicates sparse or patchy snow cover at the in situ stations. For  
357 all eight snowfall events, the observed albedo is concentrated at low values, with a  
358 median of 0.24, while WRF estimated albedo using the default Noah snow albedo  
359 scheme has higher values, with a median of 0.64. Compared with albedo estimates  
360 calculated using the default scheme, WRF estimates made using the improved scheme  
361 result in a prolonged snowmelt period, which increases the number of snowmelt  
362 samples and leads to a median albedo of 0.38, which is closer to that for the in situ  
363 observations. The mean albedo estimated from WRF using the improved scheme is 0.4,  
364 which is also closer to the observed mean of 0.3, than the mean of 0.6 calculated from  
365 WRF using the default scheme (Fig. 4a, 4b). In general, the accuracy of the WRF  
366 estimates when the new scheme is used is closely related to the observed albedo.  
367 Compared with the WRF estimates made using the default Noah scheme, the WRF  
368 estimates made using the improved scheme greatly reduce the overestimation of albedo  
369 when the observed values are below 0.6, but seem to increase the underestimation of  
370 albedo when the observed values are higher than 0.6 (Fig. 4c).

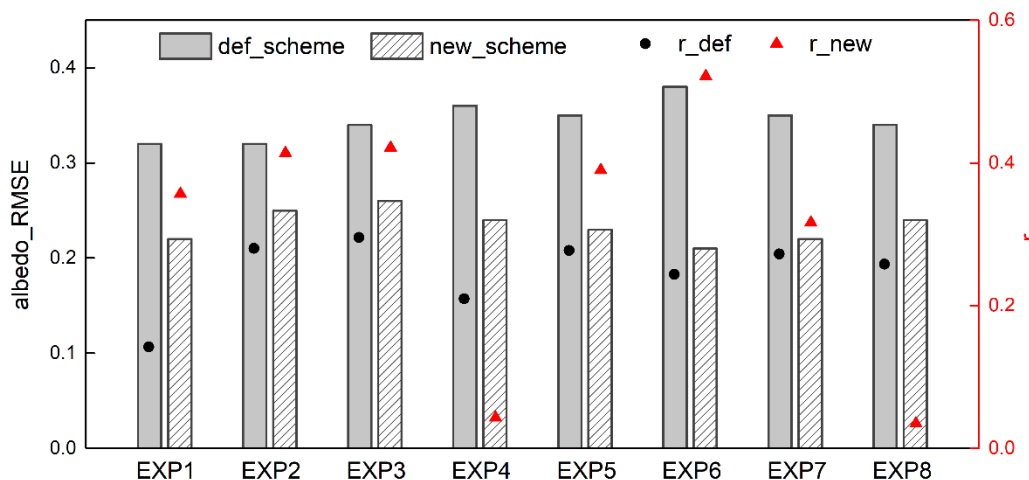


371

372 **Figure 4.** Scatterplot of albedo from observations and model estimates for the eight  
 373 experiments (a: horizontal axis denotes samples from EXP1 to EXP8), corresponding  
 374 box-and-whisker plot (b) *with lower and upper boundaries of the box indicating the*  
 375 *first and third quartiles of albedo respectively and the line inside the box indicating the*  
 376 *median of albedo, and averaged albedo observations every 0.05 segments (i.e., 0-0.049,*  
 377 *0.05-0.099, 0.1-0.149, 0.15-0.199,....., 0.85-0.899, 0.9-0.949, 0.95-0.999) and model*  
 378 *estimates at the same time as observations* for all experiments (c). For def\_scheme and  
 379 new\_scheme, see Figure 2.

380 To further evaluate the accuracy of WRF albedo estimates when the different snow  
 381 albedo schemes are used, we calculated the RMSE and correlation coefficients between  
 382 the observations and the model estimates (Figure 5). The RMSE for the WRF estimates,  
 383 when compared to the observations, ranges from 0.32 to 0.38 for the eight experiments  
 384 when the default scheme is used, and ranges from 0.21 to 0.26 when the improved  
 385 scheme is used. Compared with the default Noah snow albedo scheme, the improved  
 386 scheme results in a 0.1 decrease to the albedo RMSE in EXP1, representing a relative  
 387 decrease of 31.3 %; a 0.07 decrease in EXP2, representing a relative decrease of 21.9 %;  
 388 a 0.08 decrease in EXP3, representing a relative 23.5 % decrease; a 0.12 decrease in  
 389 EXP4 and EXP5, representing relative decreases of 33.3 % and 34.3 %, respectively; a

390 0.17 decrease in EXP6, representing a relative 44.7 % decrease; a 0.13 decrease in  
 391 EXP7, representing a relative 37.1 % decrease; and a 0.1 decrease in EXP8,  
 392 representing a relative 29.4 % decrease. With the exceptions of EXP4 and EXP8,  
 393 correlations between the modeled and observed albedo are significant at the 0.01  
 394 significance level. Implementing the improved albedo scheme in WRF increases the  
 395 albedo correlation coefficient by 0.21 in EXP1, a relative increase of 151 %; by 0.13 in  
 396 EXP2, a relative increase of 47.6 %; by 0.13 in EXP3, a relative increase of 42.5 %; by  
 397 0.11 in EXP5, a relative increase of 40.7 %; by 0.28 in EXP6, a relative increase of  
 398 114 %; and by 0.04 in EXP7, a relative increase of 16.2 % (Fig. 5). In general, during  
 399 snowfall and the snowmelt period that follows it, implementing WRF using the  
 400 improved snow albedo scheme outperforms implementing WRF using the default Noah  
 401 scheme and results in more accurate albedo estimates, demonstrated by considerable  
 402 decreases in RMSE and increases in the correlation coefficients.

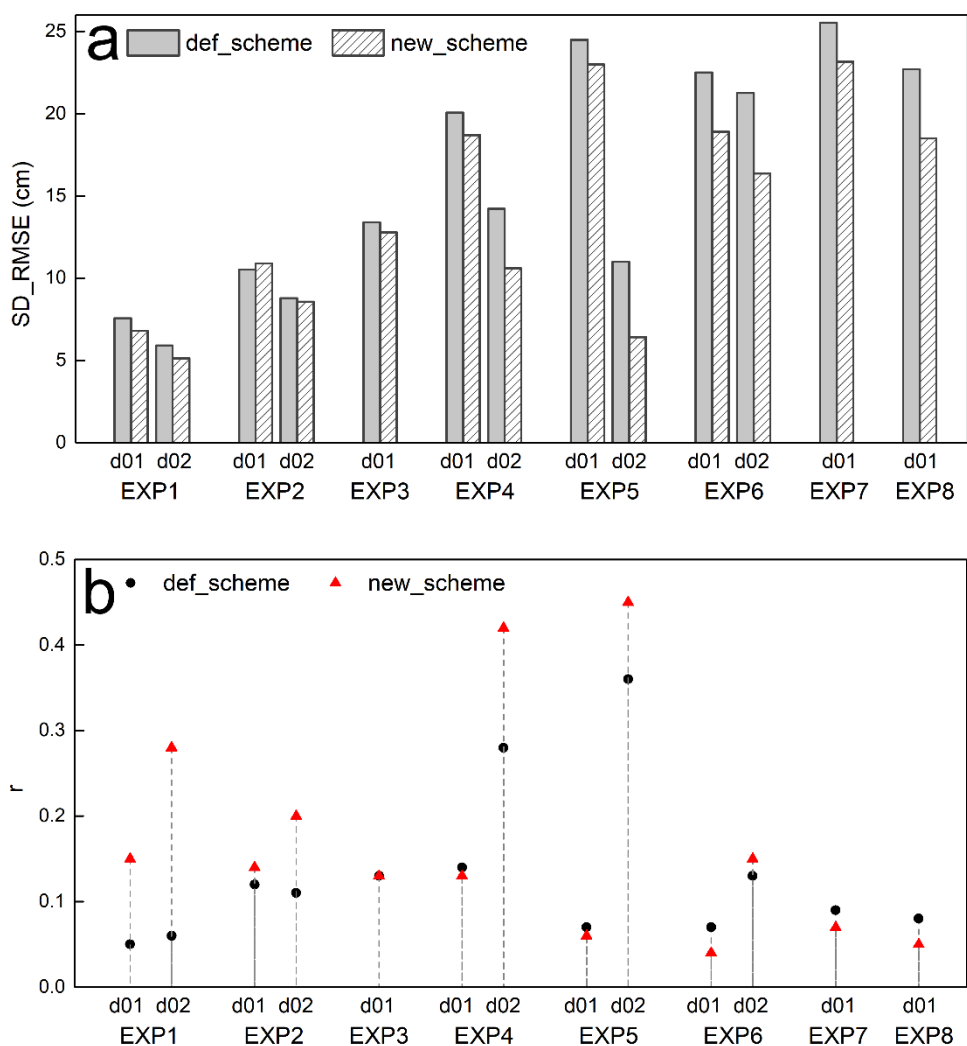


403

404 **Figure 5.** RMSE in column and correlation coefficient (r) in scatterplot for albedo,  
 405 comparing observations and model estimates. r\_def and r\_new mean r between the  
 406 observations and WRF-estimates using the default albedo scheme, and using the  
 407 improved albedo scheme, respectively. Except EXP4 and EXP8, the correlation  
 408 coefficient is significant at the 0.01 significance level. For def\_scheme and  
 409 new\_scheme, see Figure 2.

### 410 **3.3 Snow depth**

411 There is a feedback between albedo and snow. Snow accumulation and snowmelt  
412 influence the proportion of solar irradiance that is reflected; albedo indirectly and non-  
413 negligibly influences snow accumulation and snowmelt by affecting the land surface  
414 energy budget. In this study, we use an improved snow albedo scheme in which albedo  
415 is parameterized as a function of snow depth and age. WRF model estimates of albedo  
416 calculated using the improved snow albedo scheme outperform those calculated using  
417 the default Noah scheme when snowfall events are simulated, and this leads to  
418 improved representation of snowfall and the subsequent snowmelt processes in WRF  
419 when the improved scheme is used. Instantaneous direct measurements of snow depth  
420 are recorded during snowfall events and over the subsequent snowmelt period. We use  
421 these to quantify the improvement that using the new albedo scheme makes to snow  
422 estimates calculated in WRF. We assess this by calculating the RMSE and correlation  
423 coefficient between the model snow depth estimates and CMA observations, as shown  
424 in Figure 6.



425

426 **Figure 6.** Same as Figure 3, but for RMSE (a) and correlation coefficient (b) for snow  
 427 depth (SD). The correlation coefficient is significant at the 0.01 significance level,  
 428 except for d01 estimates in EXP6.

429 Comparing the accuracy of WRF snow depth estimates calculated using the new  
 430 scheme, to the accuracy achieved using the default Noah scheme, the greatest relative  
 431 decrease in RMSE is 41.7 %, which occurs for estimates made at finer resolution in  
 432 EXP5. Replacing the default albedo scheme with the new scheme in WRF results in an  
 433 average decrease in snow depth RMSE of 2.2 cm, which is a 13.4 % improvement. In  
 434 areas covered by the higher resolution model domain, the average RMSE decrease is  
 435 2.8 cm, which is a 21.2 % improvement. This shows that the impact of replacing the

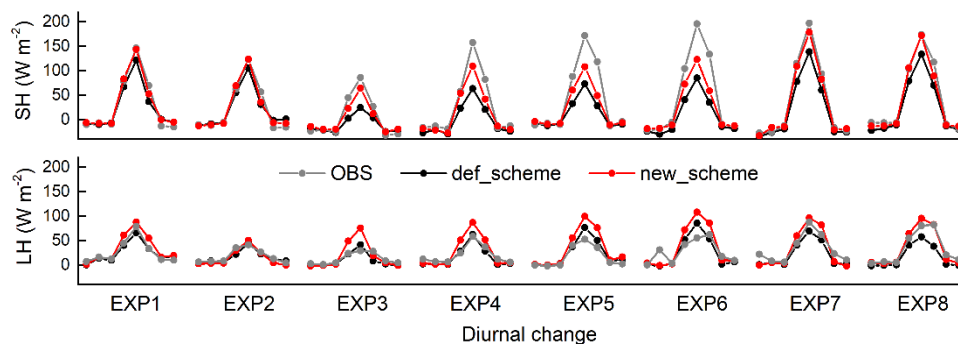
436 albedo scheme with an improved scheme is more significant for areas in the higher  
437 resolution d02 model domain than for areas in the coarser d01 model domain (Fig. 6a).  
438 Using the improved albedo scheme in WRF increases the correlation coefficient  
439 between observed and modeled snow depth in areas within the d02 model domain, but  
440 this increase is not consistent for areas in the d01 domain. The greatest increase, both  
441 relative and absolute, in the snow depth correlation coefficient occurs in the finer  
442 simulation domain in EXP1, where the correlation between observed and modeled  
443 snow depth increases by 0.22, which is a 366.7 % increase. The mean and relative  
444 increases in the correlation coefficient between observed and modeled snow depth for  
445 areas in the d02 simulations are 0.14 and 107.8 %, respectively (Fig. 6b). WRF snow  
446 depth estimates are more accurate at finer resolution (i.e., 1 km resolution) than in  
447 coarser simulations (i.e., 5 km resolution), regardless of which albedo scheme is  
448 implemented (Fig. 6). Implementing the improved albedo scheme in WRF improves  
449 the agreement between model estimated and observed snow depth, relative to  
450 implementing the default Noah albedo scheme, as seen by the decreased RMSE and the  
451 increased correlation coefficient.

### 452 **3.4 Turbulent heat and vapor fluxes**

453 Albedo plays a significant role in the land surface energy balance. It determines the  
454 proportioning of net radiation fluxes between turbulent heat and vapor fluxes. Our study  
455 shows that using the improved snow albedo scheme in WRF results in a good model  
456 representation of surface albedo in simulations of snow events. We now consider  
457 whether replacing the default scheme with the improved scheme may affect the  
458 proportioning of net radiation fluxes between turbulent heat and vapor fluxes. Since  
459 there are very few observation in situ stations located in the area covered by the finer  
460 model domain, a total of 14 in situ stations located in the area covered by d01 were  
461 selected, and WRF estimates of turbulent heat and vapor fluxes were assessed from  
462 simulations calculated at 5 km resolution (Table 2)

463 The diurnal changes in SH and LH recorded in the in situ observations and calculated

464 in the eight modeling experiments are shown in Figure 7. The WRF model successfully  
 465 captures the diurnal changes in SH and LH, particularly in EXP1 and EXP2, where the  
 466 model estimates of SH and LH are almost equal to the in situ observations. In the  
 467 nighttime, the WRF model accurately estimates SH and LH in all eight experiments.  
 468 However, during the day WRF consistently underestimates SH in all experiments  
 469 except EXP1 and EXP2, and estimates LH with varying accuracy when the default  
 470 Noah albedo scheme is used. For example, when the default Noah scheme is used, WRF  
 471 accurately estimates LH in EXP3 and EXP4, but overestimates LH in EXP5 and EXP6  
 472 and underestimates LH in EXP7 and EXP8. Compared with WRF estimates calculated  
 473 using the default scheme, WRF simulations calculated using the new albedo scheme  
 474 result in increased estimates of the turbulent heat and vapor fluxes. This leads to SH  
 475 estimates that are closer to observations for experiments EXP3 to EXP8, a greatly  
 476 overestimated LH for experiments EXP3 to EXP6, and a slightly overestimated LH,  
 477 which is closer to observations for EXP7 and EXP8 (Fig. 7). In general, WRF estimates  
 478 of SH are improved through the implementation of the new albedo scheme, relative to  
 479 the default scheme, although SH is underestimated during snowfall events. The impact  
 480 of the improved albedo scheme on LH estimates varies between the different snowfall  
 481 events, but LH is consistently overestimated.

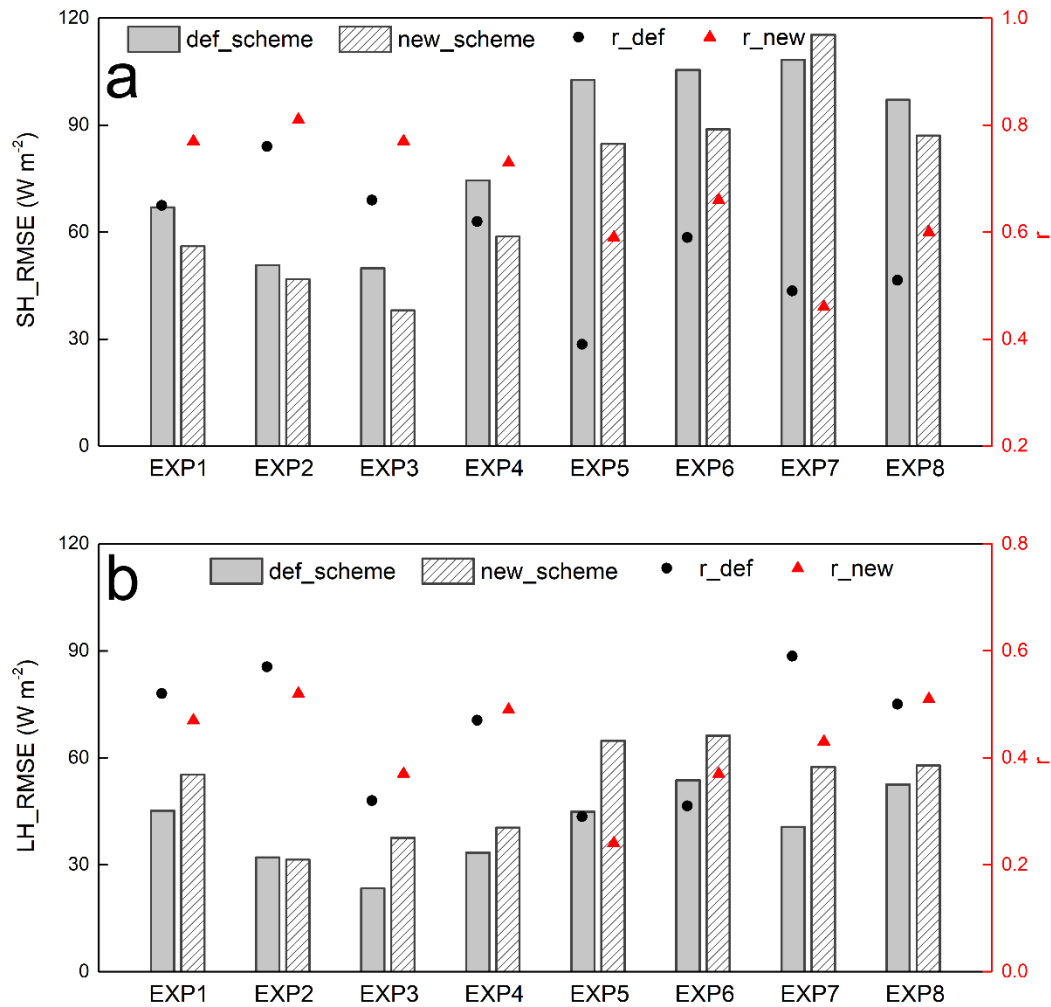


482

483 **Figure 7.** Diurnal change of sensible (SH) and latent (LH) heat fluxes from ground  
 484 observations and model estimates. Beginning at 02:00 BST with 3 hours interval. For  
 485 def\_scheme and new\_scheme, see Figure 2.

486 The RMSE and correlation coefficient for comparisons between WRF estimates and  
487 observations for SH and LH are shown in Figure 8. Compared with when the default  
488 Noah scheme is used, WRF estimates using the improved scheme result in reduced  
489 RMSE for SH estimates in all experiments except EXP7. The absolute (and relative)  
490 reductions are: 10.9 W m<sup>-2</sup> (16.2 %) in EXP1, 3.9 W m<sup>-2</sup> (7.6 %) in EXP2, 11.9 W m<sup>-2</sup>  
491 (23.8 %) in EXP3, 15.7 W m<sup>-2</sup> (21 %) in EXP4, 17.9 W m<sup>-2</sup> (17.4 %) in EXP5, 16.6 W  
492 m<sup>-2</sup> (15.8 %) in EXP6, and 10.0 W m<sup>-2</sup> (10.3 %) in EXP8. There is a relative increase  
493 of 6.5 % in EXP7. Implementing the improved scheme in WRF significantly increases  
494 the correlation coefficients between observed and modeled SH, relative to using the  
495 default scheme, in all experiments except EXP7, where there is a slight decrease. The  
496 largest increase in the SH correlation coefficient, both absolute and relative, is 0.2 and  
497 51.3 %, respectively, and occurs for EXP5. Implementing the improved scheme in WRF  
498 reduces the SH RMSE by an average of 10 W m<sup>-2</sup>, which is an improvement of 13.2 %  
499 improvement, and increases the SH correlation coefficient by an average of 0.1, which  
500 is an improvement of 16.8 % (Fig. 8a). However, replacing the default scheme with the  
501 improved albedo scheme results in less accurate estimates of LH, and corresponds to  
502 an increase in RMSE in almost all eight experiments, although the correlation  
503 coefficient increases for half of the snowfall events simulations (EXP3, EXP4, EXP6  
504 and EXP8) (Fig. 8b).

505 In summary, the improved snow albedo scheme has a significant effect on the  
506 proportioning of radiative fluxes between turbulent heat and vapor fluxes. It  
507 significantly outperforms the default Noah scheme in relation to SH estimates, but there  
508 is no significant improvement in LH estimates and these may be less accurate when the  
509 new scheme is used, relative to the default scheme, during snowfall and the subsequent  
510 snowmelt period.



511

512 **Figure 8.** Same as Figure 5, but for sensible (a) and latent (b) heat fluxes. The  
 513 correlation coefficient is significant at the 0.001 significance level.

#### 514 **4 Discussion**

515 The highly complex topography of the Tibetan Plateau means that WRF estimates of  
 516 air temperature, albedo and snow depth are strongly sensitivity to model resolution. Our  
 517 study shows that WRF performs much more accurately when run at finer resolution (1  
 518 km) than at relatively coarse resolution (5 km) for snowfall events over the Tibetan  
 519 Plateau, regardless of which snow albedo parameterization scheme is used. This  
 520 difference may be explained by the ability of the model to resolve complex terrain  
 521 (Rahimi et al., 2019), and/or by the implementation of the cumulus convective

522 parameterization scheme. The more detailed representation of complex terrain and the  
523 explicit representation of convection mean that running WRF at finer resolution greatly  
524 improves model estimates of air temperature, surface pressure, and relative humidity  
525 (Singh et al., 2020), and provides small improvements in the magnitude of daytime  
526 convective precipitation (Collier and Immerzeel, 2015). Norris et al. (2017) pointed out  
527 that decreasing the grid spacing from 6.7 to 2.2 km likely improves estimates of  
528 mountain precipitation but does not fundamentally change the representation of the  
529 diurnal cycle. They indicated that the key difference between low and high model  
530 resolution is whether or not a cumulus convective scheme is required. Subkilometer  
531 grid resolution has been investigated in WRF, and used for modeling meteorological  
532 variables over complex terrain (Horvath et al., 2012; Dimitrova et al., 2016). The 500  
533 m resolution configuration of WRF results in the closest match between the model  
534 estimates and observations, and gives the most plausible spatial distribution of  
535 precipitation over the complex topography. The performance of the WRF model has  
536 been similarly demonstrated to improve at 500 m, relative to coarser resolutions, for  
537 wind and air temperature estimates (Bonekamp et al., 2018). We therefore strongly  
538 suggest that subkilometer grid resolution should be considered when WRF is  
539 configured for simulations covering areas in High Mountain Asia in future research.

540 Our improved snow albedo scheme parameterizes albedo as a function of snow depth  
541 and age by considering the relationship between MODIS albedo and the modelled snow  
542 depth and age. It is more physically plausible than the default Noah scheme, which  
543 considers snow cover, and outperforms the default Noah scheme for air temperature,  
544 snow depth, albedo and turbulent heat and vapor fluxes estimates during snowfall  
545 events. However, even when the improved albedo scheme is used, the RMSE for WRF  
546 estimates of albedo at 5 km spatial resolution remains around 0.21-0.26, although this  
547 represents a decrease of 22-45 % relative to when the default albedo scheme is used. It  
548 should be noted that the accuracy of the MODIS albedo retrieval algorithm is limited  
549 during snowfall events and snowmelt periods (Qin et al., 2011; An et al., 2020), and  
550 also that rugged mountain terrain not only affects the radiation absorbed by the land

551 surface, but also affects the radiation reflected by the land surface to the satellite borne  
552 sensor. Multiple reflection and scattering from adjacent mountains creates challenges  
553 for the monitoring and retrieval of surface albedo in areas of complex terrain via remote  
554 sensing (Zhang and Gao, 2011; Roupioz et al., 2014, 2016). This reduces the accuracy  
555 of MODIS albedo retrieval over the complex topographic Tibetan Plateau and  
556 constitutes a limitation to the improved albedo parameterization investigated here, since  
557 it relies on MODIS albedo products. A terrain correction is required for the MODIS  
558 albedo retrieval to further improve the albedo parameterization scheme used here.  
559 However, it is difficult to establish a unified terrain correction model due to the large  
560 undulations of the Tibetan Plateau. How to effectively eliminate the influence of terrain  
561 factors from a specific mountain surface on quantitative retrievals from remote sensing  
562 data has long been a challenge and a focus for remote sensing research. A further  
563 challenge for the assessment presented here is the sparse and uneven distribution of  
564 available in situ albedo observation data over the bulk Tibetan Plateau. This paucity of  
565 data means that there is a mismatch in spatial resolution when comparing albedo  
566 estimates, calculated at 5 km resolution, with in situ observations.

567 Air temperature is a critical factor that is related to albedo and determines energy  
568 distribution between SH and LH. Using the improved snow albedo parameterization  
569 scheme significantly reduces the albedo overestimates during snowfall events that  
570 occur when the default scheme is used, and this leads to the reduction of the cold air  
571 temperature bias in the model. Therefore, in this study, the improved scheme reduces  
572 the underestimates for SH and improves the performance of WRF for simulating SH  
573 over the Tibetan Plateau, relative to when the default scheme is used. These results  
574 indicate that the accurate simulation of surface albedo is very important for the accurate  
575 simulation of SH.

576 Implementing the improved albedo scheme results in little improvement to estimates of  
577 LH calculated, which is restricted by water content and increased only slightly, relative  
578 to when the default albedo scheme is used. This may be explained by the LH

579 parameterization scheme used in the Noah LSM (Chen and Dudhia, 2001). The total  
580 LH in the Noah LSM has three components (LH from the direct evaporation from the  
581 top surface layer, evaporation of precipitation intercepted by the canopy and  
582 transpiration via the canopy and roots respectively). The factors affecting calculation  
583 of LH in the Noah LSM include not only the radiation balance (which is impacted by  
584 albedo), but also soil water, soil capillary conductivity and vegetation status, i.e., albedo,  
585 surface heat and water vapor exchange coefficient, saturated water vapor pressure,  
586 specific humidity, surface soil water content, field capacity, wilting point, canopy  
587 resistance, total precipitation, and canopy interception amount. In our current study, we  
588 have focused on the snow albedo parameterization scheme in the Noah LSM by  
589 considering the MODIS albedo product and the additional snow related variable of  
590 snow depth. Therefore, the influence of our improved scheme on LH estimates  
591 calculated by the LSM is very limited.

592 Implementing the improved snow albedo scheme in place of the default scheme greatly  
593 decreases the overestimation of albedo from snowmelt to snow free processes, but does  
594 not remove the underestimation of albedo during snowfall. This means that the  
595 improvements mainly come from snowmelt and snow free simulations, and model  
596 performance during snowfall may be worse when the improved albedo scheme is used.  
597 This suggests an opportunity to further investigate how albedo is characterized by snow  
598 depth and age in the snow albedo parameterization scheme.

## 599 **5 Conclusions**

600 We conducted several numerical experiments to evaluate the performance of the  
601 MODIS albedo based snow albedo parameterization scheme (Liu, 2020) implemented  
602 in WRF. We assessed the RMSE and correlation coefficient between observed and  
603 modeled air temperature, albedo, snow depth and turbulent heat and vapor fluxes for  
604 simulations of eight snowfall events over the Tibetan Plateau. We compared the  
605 accuracy of WRF estimates made using the improved snow albedo scheme with that of  
606 WRF estimates made using the default Noah scheme, in both cases comparing with

607 ground observations.

608 The accuracy of WRF estimates of albedo is significantly improved when the new  
609 albedo scheme is implemented. The default Noah scheme tends towards higher albedo  
610 estimates and cannot accurately capture snowfall and snowmelt processes, resulting in  
611 a high RMSE and low correlation coefficient between modeled and observed albedo.  
612 Through consideration of snow related variables, such as snow depth and age, and by  
613 being based on MODIS remote sensing albedo products, the improved scheme  
614 estimates albedo more accurately than the default scheme, improving the albedo RMSE  
615 by around 22 % to 45 %, with an average improvement of 32 %. Similarly, the improved  
616 scheme results in an increased correlation coefficient between modeled and observed  
617 albedo. Relative to the default scheme, the correlation coefficient relatively increases  
618 by around 16 % to 151 %, with an average improvement of 69 %. This may contribute  
619 to the relatively better performance of WRF for simulating air temperatures when the  
620 improved albedo scheme is used. The improved scheme relatively decreases (increases)  
621 the air temperature RMSE (correlation coefficient) by 16 % (1.5 %) for model estimates  
622 calculated at 5 km resolution, and by 27 % (5 %) for model estimates calculated at 1  
623 km resolution.

624 There are mutual feedbacks between snow and albedo. During snowfall and over the  
625 subsequent snowmelt period, snow depth and age affect changes in the albedo. The  
626 changes in albedo in turn affect the evolution of snow events by changing the surface  
627 energy budget and the proportional distribution of net radiation between turbulent heat  
628 and vapor fluxes, and finally by changing the type of precipitation. Our study shows  
629 that when the default albedo scheme is replaced by the improved albedo scheme in  
630 WRF, the turbulent heat and vapor fluxes estimates increase. The improved scheme  
631 significantly outperforms the default Noah scheme for SH estimates, with a reduction  
632 (increase) in the RMSE (correlation coefficient) of  $10 \text{ W m}^{-2}$  (0.1), representing an  
633 improvement of 13 % (17 %). The overall accuracy with which WRF estimates  
634 turbulent heat and vapor fluxes improves when the improved albedo scheme replaces

635 the default scheme, although there is no significant improvement in LH estimates. This  
636 overall improvement leads to a more accurate reproduction of the evolution of snowfall  
637 events and to more accurate snow depth estimates. Our study shows that using the  
638 improved albedo scheme in WRF reduces the RMSE and increases the correlation  
639 coefficient between modeled and observed snow depth, relative to using the default  
640 scheme. This improvement is more significant for simulations at 1 km resolution than  
641 for simulations at 5 km resolution, with maximum and averaged relative RMSE  
642 (correlation coefficient) decreases (increases) of 42 % (367 %) and 21 % (108 %),  
643 respectively for 1 km resolution simulations.

#### 644 **Acknowledgements**

645 This research was supported by the Strategic Priority Research Program of Chinese  
646 Academy of Sciences (XDA20060101), the Second Tibetan Plateau Scientific  
647 Expedition and Research program (STEP) (2019QZKK0103), the National Natural  
648 Science Foundation of China (41661144043, 91637312, 41830650, 91737205), MOST  
649 High Level Talent grant No. G20190161018, the Chinese Academy of Sciences  
650 President's International Fellowship Initiative Grant No. 2020VTA0001, the Key  
651 Research Program of Frontier Sciences of Chinese Academy of Sciences (QYZDJ-  
652 SSW-DQC019) and Key Research and Development Projects of the Ministry of  
653 Science and Technology (2018YFC1505701). The authors express thanks to ECMWF  
654 for sharing atmospheric reanalysis data set (ERA5 dataset is available from  
655 <https://www.ecmwf.int/en/forecasts/datasets/reanalysis-datasets/era5>), to NASA for  
656 offering MODIS reflectance products (<https://modis.gsfc.nasa.gov/>), and to staff from  
657 CMA, CAS and Qilian Mountains integrated observatory network for very hard work  
658 in meteorological observations and offering the data (CMA meteorological data is  
659 available from <http://data.cma.cn/en>; albedo and turbulent heat and vapor fluxes  
660 observations from CAS and Qilian Mountains integrated observatory network is  
661 provided by National Tibetan Plateau Data Center (<http://data.tpdac.ac.cn>). The first  
662 author would like to acknowledge all group members for their help in completing this

663 paper.

664 **Reference**

665 An, Y., Meng, X., Zhao, L., Li, Z., Wang, S., Shang, L., Chen, H., Lyu, S., Li, G., and  
666 Ma, Y.: Performance of GLASS and MODIS satellite albedo products in diagnosing  
667 albedo variations during different time scales and special weather conditions in the  
668 Tibetan Plateau, *Remote Sens.*, 12, 2456, 2020.

669 Aoki, T., Hachikubo, A., and Hori, M.: Effects of snow physical parameters on  
670 shortwave broadband albedos, *J. Geophys. Res.*, 108, D19, 2003.

671 Bao, Y. and Lyu, S.: Improvement of surface albedo parameterization within a regional  
672 climate model (regcm3), *Hydrol. Earth Syst. Sci.*, 6, 1651-1676, 2009.

673 Bao, Y., Lyu, S., Zhang, Y., Meng, X., and Yang, S.: Improvement of surface albedo  
674 simulations over arid regions, *Adv. Atmos. Sci.*, 25, 481-488, 2008.

675 Bloch, M. R.: Dust-induced albedo changes of polar ice sheets and glacierization, *J.*  
676 *Glaciol.*, 5, 241-244, 1964.

677 Bonekamp, P. N. J., Collier, E., and Immerzeel, W. W.: The impact of spatial resolution,  
678 land use, and spinup time on resolving spatial precipitation patterns in the Himalayas,  
679 *J. Hydrometeorol.*, 19, 1565-1581, 2018.

680 Chen, F. and Dudhis, J.: Coupling an advanced land surface-hydrology model with the  
681 Penn State-NCAR MM5 modeling system. Part I: Model implementation and  
682 sensitivity, *Mon. Weather Rev.*, 129, 569-585, 2001.

683 Collier, E. and Immerzeel, W. W.: High-resolution modeling of atmospheric dynamics  
684 in the Nepalese Himalaya, *J. Geophys. Res.*, 120, 9882-9896, 2015.

685 Dang, C., Brandt, R. E., and Warren, S. G.: Parameterizations for narrowband and  
686 broadband albedo of pure snow and snow containing mineral dust and black carbon, *J.*

687 Geophys. Res., 120, 5446-5468, 2015.

688 Dimitrova, R., Silver, Z., Zsedrovits, T., Hocut, C. M., Leo, L. S., Di Sabatino, S., and  
689 Fernando, H. J. S.: Assessment of planetary boundary-layer schemes in the Weather  
690 Research and Forecasting mesoscale model using Materhorn field data, Bound-Lay  
691 Meteorol., 159, 589-609, 2016.

692 Ek, M. B., Mitchell, K. E., Lin, Y., Rogers, E., Grunmann, P., Koren, V., Gayno, G., and  
693 Tarpley, J. D.: Implementation of Noah land surface model advances in the National  
694 Centers for Environmental Prediction operational mesoscale Eta model, J. Geophys.  
695 Res., 108, D22, 2003.

696 Gao, Y., Xu, J., and Chen, D.: Evaluation of WRF mesoscale climate simulations over  
697 the Tibetan Plateau during 1979-2011, J. Clim., 28, 2823-2841, 2015.

698 Gardner, A. S. and Sharp, M. J.: A review of snow and ice albedo and the development  
699 of a new physically based broadband albedo parameterization, J. Geophys. Res., 115,  
700 F1, 2010.

701 Hansen, J. and Nazarenko, L.: Soot climate forcing via snow and ice albedos, PNAS,  
702 101, 423-428, 2004.

703 He, C., Takano, Y., Liou, K.-N., Yang, P., Li, Q., and Chen, F.: Impact of snow grain  
704 shape and black carbon-snow internal mixing on snow optical properties:  
705 Parameterizations for climate models, J. Clim., 30, 10019-10036, 2017.

706 He, C., Liou, K.-N., and Takano, Y.: Resolving size distribution of black carbon  
707 internally mixed with snow: Impact on snow optical properties and albedo, Geophys.  
708 Res. Lett., 45, 2697-2705, 2018a.

709 He, C., Liou, K.-N., Takano, Y., Yang, P., Qi, L., and Chen, F.: Impact of grain shape  
710 and multiple black carbon internal mixing on snow albedo: Parameterization and  
711 radiative effect analysis, J. Geophys. Res., 123, 1253-1268, 2018b.

712 Horvath, K., Koracin, D., Vellore, R., Jiang, J., and Belu, R.: Sub-kilometer dynamical  
713 downscaling of near-surface winds in complex terrain using WRF and MM5 mesoscale  
714 models, *J. Geophys. Res.*, 117, D11, 2012.

715 Jonsell, U., Hock, R., and Holmgren, B.: Spatial and temporal variations in albedo on  
716 Storglaciaren, Sweden, *J. Glaciol.*, 49, 59-68, 2003.

717 Kuipers Munneke, P., van den Broeke, M. R., Lenaerts, J. T. M., Flanner, M. G.,  
718 Gardner, A. S., and van de Berg, W. J.: A new albedo parameterization for use in climate  
719 models over the Antarctic ice sheet, *J. Geophys. Res.*, 116, D5, 2011.

720 Li, X.: Qilian Mountains integrated observatory network: Dataset of Qinghai Lake  
721 integrated observatory network (eddy covariance system of Alpine meadow and  
722 grassland ecosystem Superstation, 2018), National Tibetan Plateau Data Center, 2019.

723 Li, Y. and Hu, Z.: A study on parameterization of surface albedo over grassland surface  
724 in the northern Tibetan Plateau, *Adv. Atmos. Sci.*, 26, 161-168, 2009.

725 *Liang, S.: Narrowband to Broadband conversions of land surface albedo: I. Algorithms,*  
726 *Remote Sens. Environ.*, 76, 213-238, 2000.

727 Liang, X., Xu, M., Gao, W., Kunkel, K., Slusser, J., Dai, Y., Min, Q., Houser, P. R.,  
728 Rodell, M., Schaaf, C. B., and Gao, F.: Development of land surface albedo  
729 parameterization based on Moderate Resolution Imaging Spectroradiometer (MODIS)  
730 data, *J. Geophys. Res.*, 110, D11, 2005.

731 Lin, P., Wei, J., Yang, Z., Zhang, Y., and Zhang, K.: Snow data assimilation-constrained  
732 land initialization improves seasonal temperature prediction, *Geophys. Res. Lett.*, 43,  
733 11423-11432, 2016.

734 Liu, L.: Diagnostic analysis and numerical simulation of a regional heavy snowfall over  
735 the Tibetan Plateau, Doctoral dissertation, Chapter 5, Institute of Tibetan Plateau  
736 Research, Chinese Academy of Sciences, Building 3, Courtyard 16, Lincui Road,

737 Chaoyang District, Beijing, China, 2020.

738 Liu, L., Ma, Y., Menenti, M., Zhang, X., and Ma, W.: Evaluation of WRF modeling in  
739 relation to different land surface schemes and initial and boundary conditions: A snow  
740 event simulation over the Tibetan Plateau, *J. Geophys. Res.*, 124, 209-226, 2019.

741 Liu, S., Che, T., Xu, Z., Ren, Z., Tan, J., and Zhang, Y.: Qilian Mountains integrated  
742 observatory network: Dataset of Heihe integrated observatory network (Large aperture  
743 scintillometer of Daman Superstation, 2019), National Tibetan Plateau Data Center,  
744 2020.

745 Livneh, B., Xia, Y., Mitchell, K. E., Ek, M. B., and Lettenmaier, D. P.: Noah LSM snow  
746 model diagnostics and enhancements, *J. Hydrometeorol.*, 11, 721-738, 2010.

747 Ma, Y., Wang, Y., and Han, C.: Regionalization of land surface heat fluxes over the  
748 heterogeneous landscape: from the Tibetan Plateau to the Third Pole region, *Int. J.*  
749 *Remote Sens.*, 39, 5872-5890, 2018.

750 Ma, Y., Hu, Z., Xie, Z., Ma, W., Wang, B., Chen, X., Li, M., Zhong, L., Sun, F., Gu, L.,  
751 Han, C., Zhang, L., Liu, X., Ding, Z., Sun, G., Wang, S., Wang, Y., and Wang, Z.: A  
752 long-term (2005-2016) dataset of hourly integrated land-atmosphere interaction  
753 observations on the Tibetan Plateau, *Earth Syst. Sci. Data*, 12, 2937-2957, 2020.

754 Malik, M. J., van der Velde, R., Vekerdy, Z., and Su, Z.: Improving modeled snow  
755 albedo estimates during the spring melt season, *J. Geophys. Res.*, 119, 7311-7331, 2014.

756 Maussion, F., Scherer, D., Finkelnburg, R., Richters, J., Yang, W., and Yao, T.: WRF  
757 simulation of a precipitation event over the Tibetan Plateau, China-an assessment using  
758 remote sensing and ground observations, *Hydrol. Earth Syst. Sci.*, 15, 1795-1817, 2011.

759 Meng, C. and Li, H.: Solar radiation partitioning and surface albedo parameterization  
760 in the hinterland of Taklimakan Desert, *Adv. Meteorol.*, 1-8, 2019.

761 Meng, X., Lyu, S., Zhang, T., Zhao, L., Li, Z., Han, B., Li, S., Ma, D., Chen, H., Ao, Y.,

762 Luo, S., Shen, Y., Guo, J., and Wen, L.: Simulated cold bias being improved by using  
763 MODIS time-varying albedo in the Tibetan Plateau in WRF model, *Environ. Res. Lett.*,  
764 13, 44028, 2018.

765 Norris, J., Carvalho, L. M. V., Jones, C., Cannon, F., Bookhagen, B., Palazzi, E., and  
766 Tahir, A. A.: The spatiotemporal variability of precipitation over the Himalaya:  
767 Evaluation of one-year WRF model simulation, *Clim. Dynam.*, 49, 2179-2204, 2017.

768 Oerlemans, J. and Knap, W. H.: A 1 year record of global radiation and albedo in the  
769 ablation zone of Morteratschgletscher, Switzerland, *J. Glaciol.*, 44, 231-238, 1998.

770 Park, S. and Park, S. K.: Parameterization of the snow-covered surface albedo in the  
771 Noah-MP version 1.0 by implementing vegetation effects, *Geosci. Model Dev.*, 9, 1073-  
772 1085, 2016.

773 Qin, J., Yang, K., Liang, S., Zhang, H., Ma, Y., Guo, X., and Chen, Z.: Evaluation of  
774 surface albedo from GEWEX-SRB and ISCCP-FD data against validated MODIS  
775 product over the Tibetan Plateau, *J. Geophys. Res.*, 116, D24, 2011.

776 Rahimi, S. R., Wu, C., Liu, X., and Brown, H.: Exploring a variable-resolution  
777 approach for simulating regional climate over the Tibetan Plateau using VR-CESM, *J.*  
778 *Geophys. Res.*, 124, 4490-4513, 2019.

779 Rai, A., Saha, S. K., and Sujith, K.: Implementation of snow albedo schemes of varying  
780 complexity and their performances in offline Noah and Noah coupled with NCEP  
781 CFSv2, *Clim. Dynam.*, 53, 1261-1276, 2019.

782 Roupioz, L., Nerry, F., Jia, L., and Menenti, M.: Improved surface reflectance from  
783 remote sensing data with sub-pixel topographic information, *Remote Sens.*, 6, 10356-  
784 10374, 2014.

785 Roupioz, L., Jia, L., Nerry, F., and Menenti, M.: Estimation of daily solar radiation  
786 budget at kilometer resolution over the Tibetan Plateau by integrating MODIS data

787 products and a DEM, *Remote Sens.*, 8, 2016.

788 Saito, M., Yang, P., Loeb, N. G., and Kato, S.: A novel parameterization of snow albedo  
789 based on a two-layer snow model with a mixture of grain habits, *J. Atmos. Sci.*, 76,  
790 1419-1436, 2019.

791 Sellers, P. J., Randall, D. A., Collatz, G. J., Berry, J. A., Field, C. B., Dazlich, D. A.,  
792 Zhang, C., Collelo, G. D., and Bounoua, L.: A revised land surface parameterization  
793 (SiB2) for atmospheric GCMs. Part I: Model formulation, *J. Clim.*, 9, 676-705, 1996.

794 Skamarock, W., Klemp, J. B., Dudhia, J., Gill, D. O., Barker, D. M., Wang, W., and  
795 Powers, J. G.: A description of the advanced research WRF version 3, NCAR Technical  
796 Note NCAR/TN-475+STR, 2008.

797 Singh, J., Singh, N., Ojha, N., Sharma, A., Pozzer, A., Kiran Kumar, N., Rajeev, K.,  
798 Gunthe, S. S., and Kotamarthi, V. R.: Effects of spatial resolution on WRF v3.8.1  
799 simulated meteorology over the central Himalaya, *Geosci. Model Dev.*, 2020.

800 Wang, J., Cui, Y., He, X., Zhang, J., and Yan, S.: Surface albedo variation and its  
801 influencing factors over Dongkemadi glacier, central Tibetan Plateau, *Adv. Meteorol.*,  
802 852098, 2015.

803 Wang, W., Yang, K., Zhao, L., Zheng, Z., Lu, H., Mamtimin, A., Ding, B., Li, X., Zhao,  
804 L., Li, H., Che, T., and Moore, J. C.: Characterizing surface albedo of shallow fresh  
805 snow and its importance for snow ablation on the interior of the Tibetan Plateau, *J.*  
806 *Hydrometeorol.*, 21, 815-827, 2020.

807 Wang, Z., Zeng, X., and Barlage, M.: Moderate Resolution Imaging Spectroradiometer  
808 bidirectional reflectance distribution function-based albedo parameterization for  
809 weather and climate models, *J. Geophys. Res.*, 112, 2007.

810 Warren, S. G. and Wiscombe, W. J.: A model for the spectral albedo of snow .II: Snow  
811 containing atmospheric aerosols, *J. Atmos. Sci.*, 37, 2734-2745, 1980.

812 Wen, J., Su, Z., Tian, H., Shi, X., Zhang, Y., Wang, X., Liu, R., Zhang, T., Kang, Y.,  
813 Lyu, S., and Zhang, J.: Advances in observation and modeling of land surface processes  
814 over the source region of the Yellow River, *Advances in Earth Science*, 26, 575-585,  
815 2011.

816 Wiscombe, W. J. and Warren, S. G.: A model for the spectral albedo of snow. I: Pure  
817 snow, *J. Atmos. Sci.*, 37, 2712-2733, 1980.

818 Xu, J. and Shu, H.: Assimilating MODIS-based albedo and snow cover fraction into the  
819 common land model to improve snow depth simulation with direct insertion and  
820 deterministic ensemble Kalman filter method, *J. Geophys. Res.*, 119, 10684-10701,  
821 2014.

822 Xue, Y., Houser, P. R., Maggioni, V., Mei, Y. W., Kumar, S. V., and Yoon, Y.:  
823 Assimilation of satellite-based snow cover and freeze/thaw observations over high  
824 mountain Asia, *Front. Earth Sci.*, 7, 2019.

825 Yuan, W., Xu, W., Ma, M., Chen, S., Liu, W., and Cui, L.: Improved snow cover model  
826 in terrestrial ecosystem models over the Qinghai-Tibetan Plateau, *Agr. For. Meteorol.*,  
827 218, 161-170, 2016.

828 Zhang, W. and Gao, Y.: Topographic correction algorithm for remotely sensed data  
829 accounting for indirect irradiance, *Int. J. Remote Sens.*, 32, 1807-1824, 2011.

830 Zhang, Y., Hoar, T. J., Yang, Z., Anderson, J. L., Toure, A. M., and Rodell, M.:  
831 Assimilation of MODIS snow cover through the data assimilation research testbed and  
832 the community land model version 4, *J. Geophys. Res.*, 119, 7091-7103, 2014.

833 Zhao, C. and Zhang, R.: Cold and Arid Research Network of Lanzhou university (eddy  
834 covariance system of Guazhou station, 2019), National Tibetan Plateau Data Center,  
835 2020.

836 Zhong, E., Li, Q., Sun, S., Chen, W., Chen, S., and Nath, D.: Improvement of a snow

837 albedo parameterization in the snow–atmosphere–soil transfer model: Evaluation of  
838 impacts of aerosol on seasonal snow cover, *Adv. Atmos. Sci.*, 34, 1333-1345, 2017.